

Image Deblurring by Exploring In-depth Properties of Transformer

Pengwei Liang, Junjun Jiang, *Senior Member, IEEE*, Xianming Liu, *Member, IEEE*, and Jiayi Ma, *Senior Member, IEEE*

Abstract—Image deblurring continues to achieve impressive performance with the development of generative models. Nonetheless, there still remains a displeasing problem if one wants to improve perceptual quality and quantitative scores of recovered image at the same time. In this study, drawing inspiration from the research of transformer properties, we introduce the pretrained transformers to address this problem. In particular, we leverage deep features extracted from a pretrained vision transformer (ViT) to encourage recovered images to be sharp without sacrificing the performance measured by the quantitative metrics. The pretrained transformer can capture the global topological relations (*i.e.*, self-similarity) of image, and we observe that the captured topological relations about the sharp image will change when blur occurs. By comparing the transformer features between recovered image and target one, the pretrained transformer provides high-resolution blur-sensitive semantic information, which is critical in measuring the sharpness of the deblurred image. On the basis of the advantages, we present two types of novel perceptual losses to guide image deblurring. One regards the features as vectors and computes the discrepancy between representations extracted from recovered image and target one in Euclidean space. The other type considers the features extracted from an image as a distribution and compares the distribution discrepancy between recovered image and target one. We demonstrate the effectiveness of transformer properties in improving the perceptual quality while not sacrificing the quantitative scores (PSNR) over the most competitive models, such as Uformer, Restormer, and NAFNet, on defocus deblurring and motion deblurring tasks.

Index Terms—Image deblurring, Vision transformer, Perceptual loss, Off-the-shelf representations

I. INTRODUCTION

IMAGE deblurring is a long-standing problem in low-level computer vision, which aims to recover a sharp image from a blurred input [1]. There are various factors that can lead to the blurry. For instance, defocus blurring arises when depth variation goes beyond the allowable range of focus [2]; motion blur is caused by camera shakes or object motions during the exposure in dynamic environments [3]. The complicated degradation process makes it very challenging to accurately estimate the blur kernel by formulating the image deblurring as an inverse filtering kernel problem. To avoid explicitly estimating the blur kernel, it has become popular for deblurring methods to directly recover the sharp image from the blur image via an end-to-end learning way. Recently, a variety of

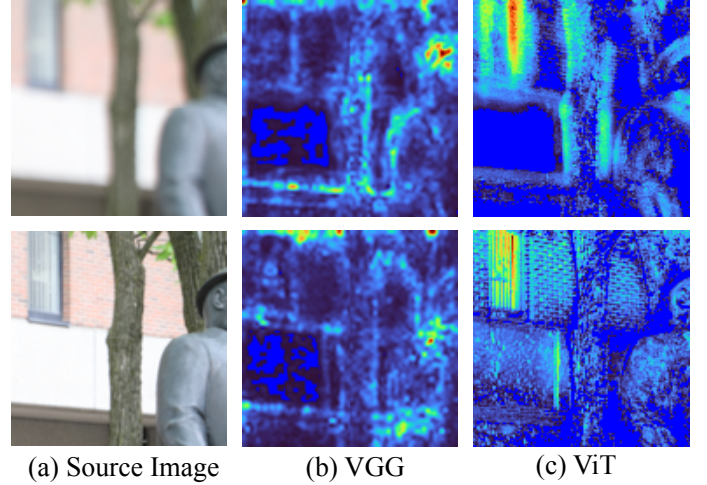


Fig. 1: Illustration the effectiveness of VGG and ViT features. The first row presents a blurry example and its feature representations; The second row shows the ground truth and corresponding visualization of features. By comparing the visualized features of the last column, we can observe that the image blur obviously changes the topological relations (*i.e.*, self-similarity) of features extracted from the clean images.

end-to-end methods have been proposed that have achieved promising performance. It is worth noting that most of these deblurring studies use pixel-wise loss functions such as ℓ_1 or ℓ_2 to minimize the distance between recovered images and reference images [4], [5], [6], [7], [8].

However, the pixel-wise losses will suffer from some limitations when handling the image blind deblurring task. Most commonly, the losses of ℓ_1 and ℓ_2 tend to drive the model to produce a blurred prediction with poor perceptual quality. To address this deficiency, Johnson *et al.* [9] introduced a perceptual loss (notated as the classical perceptual loss) as an additional regularization term into the image restoration optimization. The classical perceptual loss uses high-level features extracted from the pretrained VGG network to capture perceptual differences between the reconstructed image and ground truth. However, the improvement of visual quality is always accompanied by a decrease in quantitative metrics (*e.g.*, peak signal-to-noise ratio (PSNR)) [10], [11]. This has been avowed by many low-level vision tasks [12], [13], [1].

In this paper, we thoroughly study how to improve the perceptual quality of the deblurred image without sacrificing

P. Liang, J. Jiang and X. Liu are with the School of Computer Science and Technology, Harbin Institute of Technology, Harbin 150001. E-mail: {jiangjunjun, csxm}@hit.edu.cn.

J. Ma is with the Electronic Information School, Wuhan University, Wuhan 430072, China. E-mail: jyima2010@gmail.com.

the quantitative scores. Existing methods usually adopt the pretrained VGG as the off-the-shelf feature extractor, while the extracted feature maps are of very low resolutions. In particular, Zhang *et al.* [14] calculated the classical perceptual loss using features before the pool5 layer of VGG for motion deblurring. The size of feature maps is $32\times$ smaller than the source input. Such high-level feature maps with low spatial resolution inevitably miss rich details and provide poorly localized global semantic information [15], as shown in Fig. 1. Moreover, coarse feature maps from VGG might work well in abstract high-level tasks, but they may not be helpful in guiding image restoration in low-level vision tasks. To better guide the image deblur task, we introduce the pretrained transformer to replace the CNN-based network due to the following three factors. First, due to the global self-attention mechanism, the transformer can model the similarity of natural images well, and this is very important for the low-level image restoration task [16]. Second, unlike VGG where the resolution of the feature map gradually decreases as layers go deeper, the vision transformer (ViT) [17] maintains the same spatial resolution through all layers. Third, recent works [15], [18] reveal that even representations extracted from the last layer of ViT can still reconstruct the original image. It indicates that the features extracted from ViT preserve significantly fine-grained information in each layer.

Motivated by the above observations, we design two types of perceptual losses with the features extracted from the pretrained transformer from the local and global perspectives, respectively. Precisely, for the first type, we locally consider the element-wise features as vectors in Euclidean space and then directly compute their differences. For the second type, instead of aligning the element-wise feature at each position, we compare the global distribution of features based on the Optimal Transport (OT) theory [19]. The first loss focuses on aligning the local feature information, which may facilitate to generate deblurred image with few artifacts. While the strict constraint may limit the deblurred image to generate more details. The latter compares the distribution of features, which may produce more realistic images. However, the recovered details with global perceptual loss may not be located at the exact same spatial position as in the reference image.

The main contribution of this work is incorporating transformer properties into image deblurring task, which improves the perceptual quality of the reconstructed image, while rarely arising performance drop in quantitative metrics (*e.g.*, PSNR). We carefully investigate how to design novel perceptual losses to guide image deblurring. Extensive experiments demonstrate that the proposed perceptual losses can effectively boost the performance when applied to the most competitive approaches. Furthermore, we show that the proposed perceptual losses are general can be easily combined with other losses.

II. RELATED WORK

A. Image Deblurring

According to the nature of blur, image blur can be classified into defocus blur and motion blur [1]. In the deep learning era, a variety of deblurring methods have been proposed to address

the problem. To be specific, Abuolaim and Brown [4] provided a large-scale dataset, called DPDD, for the defocus deblurring task. In addition to the standard benchmark dataset, they also proposed a simple U-Net-like architecture as a baseline. At a later time, they further introduced a multi-decoder network architecture to improve the performance of deblurring [20]. Recently, more and more powerful network modules have been designed for defocus deblurring, including transformer block [5], [6], image representation [21], iterative filter adaptive module [22], and kernel design [23], [24], [25]. Besides, since the defocus blur is related to the depth variation, some works estimate the defocus map based on physical rules to guide the network to handle the non-uniform blur [26], [8], [27]. Compared to the defocus blur, motion blur has attracted more widespread attention in the early days. Specifically, Nah *et al.* [28] first proposed a DeepDeblur that directly maps the blurry image into its sharp counterpart without explicit kernel estimation in 2017. Several novel techniques have been successfully adopted in motion deblurring, such as multi-scale network [28], [29], scale-recurrent architectures [30], [31], adversarial training [32], [33], [34], [35], spatial frequency domain [36], reblurring [10], [14], [37], event sensor [38], and coarse-to-fine strategies [39]. Nevertheless, those methods focus on designing the network architectures and rarely explore improving image quality in terms of quantitative and perceptual measurements by designing novel losses.

B. Perceptual Loss in Image Restoration

The classical loss is introduced by Johnson *et al.* [9] for style transfer and super-resolution. The classical perceptual loss depends on high-level features extracted from pretrained VGG networks to capture latent semantic knowledge. By training with classical perceptual loss, the model can produce more visually pleasing results. Then, perceptual loss became popular in the computer vision community and spread into numerous image restoration tasks, such as image reflection removal [40], image dehazing [41], and image deblurring [14]. Inspired by the classical perceptual loss, Zhang *et al.* [42] further conducted broad experiments and revealed that intermediate deep features can model low-level perceptual similarity surprisingly well. Based on experimental observations, they proposed an image quality assessment metric, *i.e.*, learned perceptual image patch similarity (LPIPS). The most commonly used perceptual loss is to penalize the Euclidean distance between feature maps extracted from pretrained VGG [12]. In addition to computing the element-wise distance of extracted feature maps, Delbracio *et al.* [11] proposed to compare feature distributions between predicted and target images by projecting the multidimensional feature space into one dimension.

However, some work found that the performance of the quantitative measure (*e.g.*, PSNR) decreases when the classical perceptual loss is introduced to improve the perceptual quality of recovered images [12], [13], [1]. Therefore, the authors have to tune the weight of perceptual loss very carefully to maximize perception gain and minimize the decrease in quantitative scores. In this paper, we address this limitation

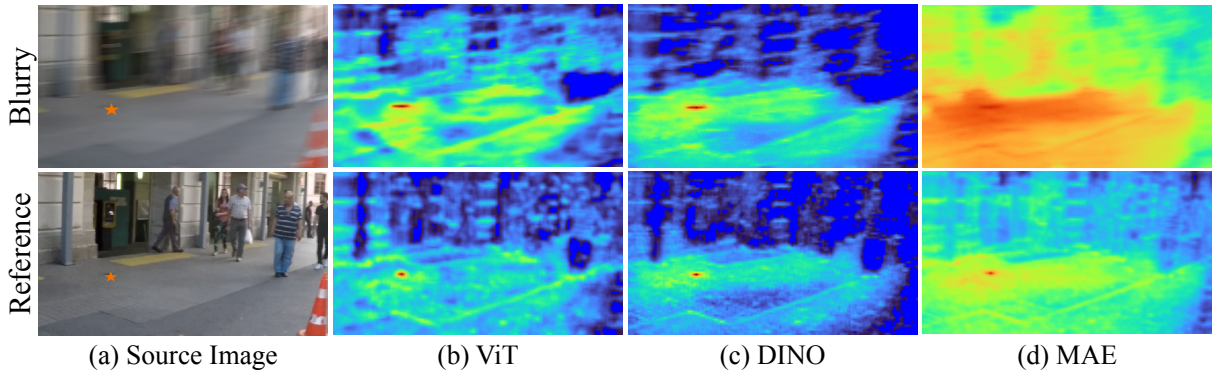


Fig. 2: Similarity visualization of different ViT features on the image deblurring dataset. We extract the ViT features from the same ViT architecture training in different ways: (b) supervised ViT [17], (c) self-supervised DINO [43], and (d) MAE [44]. The (b-d) show similarity heatmaps that are computed between a feature located at \star and all features in this image. The closer the color is to red, the higher the similarity.

using transformer feature representations extracted from pre-trained masked autoencoder (MAE) [44]. Different from the pretrained VGG, the pretrained transformer shows surprising properties in which intermediate features preserve almost all details and exhibit high-resolution blur-sensitive information. Next, we simply review the vision transformer (ViT) properties revealed in high-level vision tasks.

C. Transformer Properties in High-level Vision Tasks

As ViT has shown impressive performance across numerous high-level vision tasks, it attracts more attention to intrigue properties of ViT. Naseer *et al.* [45] presented that supervised ViT shows promising robustness properties in occlusions, adversarial attacks, and shape recognition. They also found that off-the-shelf supervised ViT features exhibit strong generalizability to new classification and recognition domains. Following this work, Amir *et al.* [15] explored the properties of a self-supervised ViT (DINO-ViT). They demonstrated that the DINO-ViT (abbreviated as DINO in the following sections) has learned more powerful visual representations encoding high spatial resolution semantic information compared to supervised ViT and pretrained CNN. Then, the authors extract the deep features from DINO as dense ViT descriptors that are applied to image retrieval, object segmentation, and copy detection applications. Even using only the ViT descriptors, they achieved competitive results on those tasks without any additional training or fine-tuning. In addition, Cao *et al.* [46] proved that each token in MAE has learned global inter-token topological relations using rigorous mathematical theory.

However, the above-mentioned studies pay more attention to high-level semantic representation understanding. It is not determined whether the abstracted representations of ViTs are useful for low-level tasks or not. In this paper, we are an effort to explore the effectiveness of ViT properties on low-level image restoration tasks.

III. METHOD

A. In-depth Transformer Properties

To verify the effectiveness of transformer properties for image deblurring, we show an example in Fig. 2, which

demonstrates that ViT features can provide fine-grained blur-sensitive guidance at higher spatial resolution. It is observed that the similarity heatmaps in a pair of blurred and sharp images are different, indicating that the blur can distort the original global self-similarity. As shown in Fig. 2(a), the highlighted position marked by \star in the clear image shows a slight difference compared to the neighborhood regions, while the difference is hard to distinguish in the blurred image. Fortunately, the difference can be significantly revealed by the ViT features, especially the MAE [44] shown in Fig. 2(d). In the similarity heatmap provided by MAE, the features at the marked position show highly similarity to a large area of blurry image. On the contrary, the features of clear image at same marked position show low similarity to neighboring areas.

Based on the observation, we can derive that minimizing the distance of transformer features provides a novel supervision for image deblurring. It should be noted that the MAE features show more salient semantic attention than the other two networks. On this basis, we employ the MAE to preserve the global self-similarity that is used to measure the disparity between the deblurred image and the reference image. Furthermore, we conduct an ablation study to analyze the effectiveness of the three types of ViT features in Sec. IV-D1.

B. Vision Transformer

Since vision transformers have been widely used as backbone networks in recent studies, we first simply review the overview of ViT. For the 2D image I , ViT projects I as a sequence of 1D patch embeddings $T = \{t_i \mid i = 1, \dots, n\}$, where n is the total number of patches. Each patch embedding t_i corresponds to a fixed-size patch of I . In addition, position embeddings are added to the patch embeddings to retain positional information about patches. In addition to position embeddings, a patch embedding used for classification is also included as an additional learnable embedding, *i.e.* $[\text{CLS}]$, which serves as the global image representation. We refer to complete embeddings as a set of tokens $T = \{t_i \mid i = \text{CLS}, 1, \dots, n\}$.

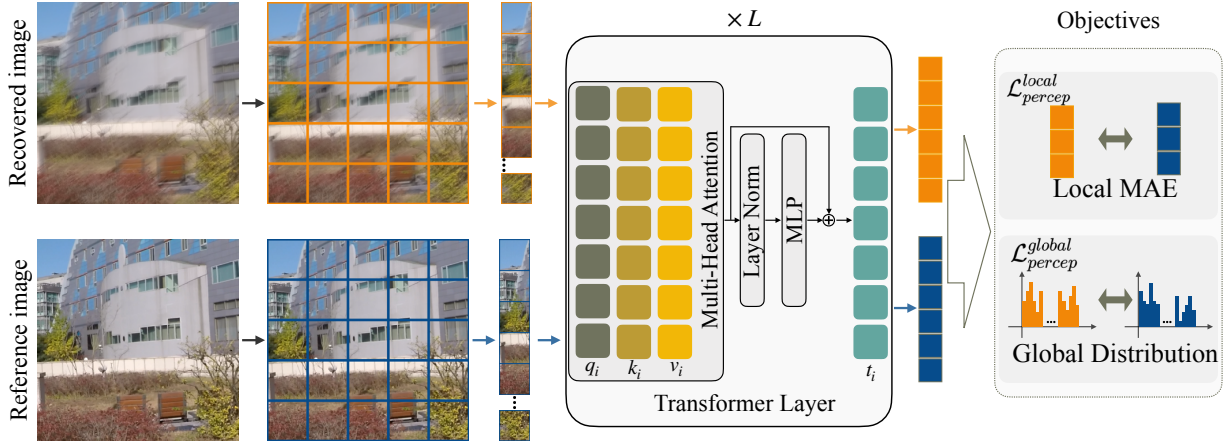


Fig. 3: The workflow illustration of proposed perceptual losses.

Then, the tokens T are passed through the transformer encoder consisting of a stack of transformer layers. For each transformer layer, there are normalization layers (LN), multi-head self-attention (MSA) modules, and multi-layer perceptron (MLP) blocks. The output of tokens in $(l+1)$ -th transformer layer can be formulated as:

$$\begin{aligned} T^{l+1} &= MSA(LN(T^l)) + T^l \\ T^{l+1} &= MLP(LN(T^{l+1})) + T^{l+1}. \end{aligned} \quad (1)$$

Precisely, in MSA block, tokens are projected into queries, keys, and values:

$$\begin{aligned} Q^{l+1} &= T^l \cdot W_q^{l+1} \\ K^{l+1} &= T^l \cdot W_k^{l+1} \\ V^{l+1} &= T^l \cdot W_v^{l+1}, \end{aligned} \quad (2)$$

where $W_q^{l+1}, W_k^{l+1}, W_v^{l+1}$ are learnable weights.

When feeding an image into a pretrained ViT model, we can obtain a set of feature representation $\{T^{l+1}, Q^{l+1}, K^{l+1}, V^{l+1}\}$ w.r.t. its token, query, key, and value, respectively. In our framework, we leverage MAE, in which the model can generate feature representation using part of image patches, that is, the number of T^{l+1} can be smaller than n .

C. Local MAE Perceptual Loss

In image deblurring task, most state-of-the-art (SoTA) deep-learning based deblurring methods focus on designing a network architecture that takes the blurry image as input and outputs the recovered image. Regarding the objective of optimization, the model minimizes the distance in spatial space between the reconstructed image I_{recon} and the reference image I_{ref} :

$$\mathcal{L}_{deblur} = h(I_{recon} - I_{ref}). \quad (3)$$

To obtain better quality of the reconstruction image, it is critical to improve the perceptual score of recovered images.

On this basis, we add a perceptual loss term into Eq. 3 using feature representation of transformer:

$$\mathcal{L}_{total} = \mathcal{L}_{deblur} + \lambda \mathcal{L}_{percep}, \quad (4)$$

where λ is a balance factor that controls the importance of the regularization term \mathcal{L}_{percep} .

The key to perceptual loss is how to use the feature representation to measure the perceptual quality of the deblurred image. Intuitively, we build a local perceptual loss using MAE feature representation inspired by the VGG-based perceptual loss [9], as shown in Fig. 3(a). We fed the reconstructed image I_{recon} and the reference image I_{ref} into pretrained MAE to extract the representations, as described in Sec. III-B. Then, we define the local perceptual loss as the Euclidean distance between feature representations:

$$\mathcal{L}_{percep}^{local} = \|\mathcal{F}^l(I_{recon}) - \mathcal{F}^l(I_{ref})\|_1, \quad (5)$$

where \mathcal{F}^l denotes the MAE backbone, which produces representations in set $\{T^l, Q^l, K^l, V^l\}$. Different from the CNN, the shadow layers of the transformer incline to capture local semantic information, while the deeper layers favor to present the global semantic information. Therefore, it is worth noting that the hyperparameter l plays a key role in the balance of local and global semantic information. The smaller l , the less perceptual information is extracted by the MAE. The bigger the l , the less attention the loss $\mathcal{L}_{percep}^{local}$ pays to quantitative scores of deblurred images. See Sec. IV-D3 for more analysis about the impact of hyperparameter l .

D. Global Distribution Perceptual Loss

Apart from computing the distance of feature vectors in Euclidean space, we also compare feature distributions between the reconstructed image and reference image based on optimal transport theory. For two sets of feature distributions, the goal of optimal transport is to minimize the cost of transporting the input into the reference distribution. When the cost is defined, the optimal transport establishes a distance between distributions, i.e., p-Wasserstein distance [47]. In other words,

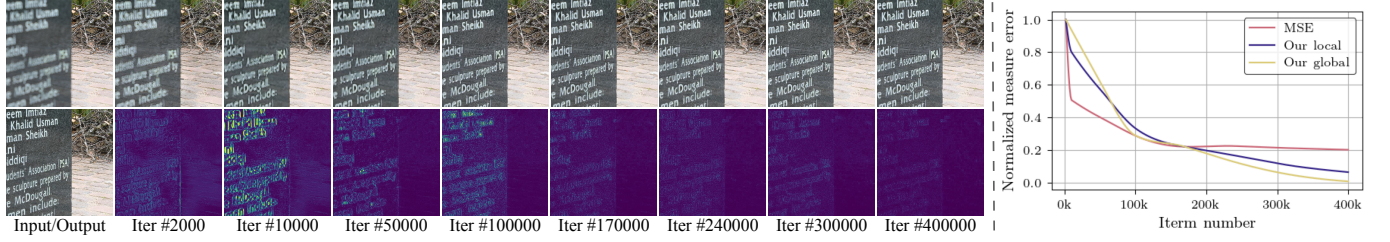


Fig. 4: Illustration of the prediction error measured by quantitative and perceptual measurement at different iterations of deblurring. To highlight the improvement in deblurring results, we show the residual maps that reflect the difference in deblurring results between the current iteration and the previous iteration.

our proposed distribution perceptual loss is equal to the p-Wasserstein distance between the reconstruction and reference distributions.

Let $\mathcal{F}^l(I_{recon})$ and $\mathcal{F}^l(I_{ref})$ denote the extracted features of the reconstructed image I_{recon} and the reference image I_{ref} in the l -th layer of the MAE encoder. To better illustrate the properties of the transformer feature, we take the token features $T_{I_{recon}}^l, T_{I_{ref}}^l$ from $\mathcal{F}^l(I_{recon})$ and $\mathcal{F}^l(I_{ref})$ as the example in the next. The token features T^l consist of $n+1$ token $t_i^l \in \mathbb{R}^d$, where each token t_i^l embeds the global topological relations [46]. Furthermore, inverting the specific token in the last layer can generate images similar to the input [18]. It demonstrates that each token can be regarded as a set of samples drawn from the distribution.

Based on above considerations, we compare the two distributions at the token feature scale, i.e., $\{t_i, k_i, q_i, v_i\}$. Within token feature scale, numerical computation is facilitative as the one-dimensional Wasserstein distance has a closed-form solution:

$$W_p^p(\mathbf{u}, \mathbf{v}) = \left(\sum_{i=1}^d |u_{i_s} - v_{i_s}|^p \right)^{\frac{1}{p}}, \quad (6)$$

where $\mathbf{u} = \{u_i\}_{i=1}^d$ denotes a set of 1D features, and u_{i_s} represents an ordered sample sorted in ascending order within \mathbf{u} , i.e., $u_{i_s} < u_{i_s+1}$ (and similarly for v_{i_s}). This implies that, for the comparison of one-dimensional empirical distributions, we can calculate the Wasserstein distance simply by sorting the samples. After computing the Wasserstein distances of all tokens, we can obtain the distribution perceptual loss that is expressed as the sum of Wasserstein distances over the $\mathcal{F}^l(I_{recon})$ and $\mathcal{F}^l(I_{ref})$:

$$\mathcal{L}_{percep}^{global} = \sum_{i=1, \dots, n, CLS} W_p^p(\mathcal{F}_i^l(I_{recon}), \mathcal{F}_i^l(I_{ref})), \quad (7)$$

where $\mathcal{F}_i^l(I_{recon})$ is one of the extracted features from $\mathcal{F}^l(I_{recon})$, i.e., $\{t_i, k_i, q_i, v_i\}$; and similarly for $\mathcal{F}_i^l(I_{ref})$. In Fig. 3(b), we show an example to explain how to measure the distance between the reconstruction and reference distributions.

As shown in Fig. 4, we present an example to illustrate the effectiveness of losses in the deblurring process. For traditional ℓ_2 loss, it is hard to reduce the measurement error as the number of iterations increases. Especially, in the last few iterations (i.e., Fig. 4 iteration 240k-400k), the values on the y-axis tend to be consistent. While we found that the measured

error continues to decrease under the two proposed types of perceptual losses measurement in Sec III-C and Sec III-D. It indicates that the perceptual quality of deblurred results continues to improve, even though the quantitative loss (ℓ_2) suffers from premature convergence. Furthermore, we show the residual maps to highlight the differences among multiple iterations. The residual maps in the last few iterations depict that characters containing more semantic information tend to receive more attention. As a result, the deblurred results look clearer from the human views.

IV. EXPERIMENTS

In this section, we introduce our experiments settings and implementation details before evaluating the performance of proposed perceptual losses in various image deblurring scenarios, including defocus deblurring and motion deblurring. Then, we conduct ablation studies to further demonstrate the benefit of perceptual loss with different transformer properties.

A. Settings and Details

1) *Dataset*: We evaluate the performance of our method on three representative datasets for defocus deblurring and motion blurring, respectively. The datasets are as follows:

DPDD. The DPDD dataset [4] provides real defocus blur and all-in-focus pairs captured with a DSLR camera. There are 500 indoor/outdoor scenes in the DPDD dataset where each scene contains two blurred sub-aperture views (left and right views) stored in lossless 16-bit depth. The DPDD dataset is divided into three sub-datasets: training, validation, and testing datasets, consisting of 350, 74, and 76 pairs, respectively. Note that we can easily obtain the single defocus blur image by averaging the two blur sub-aperture views.

GoPro. The GoPro dataset [28] is a synthetic dataset in which the synthetic blurry images are simulated from a high frame rate video captured by a high-speed camera, i.e., GoPro. By averaging consecutive short-exposure frames, blurry images that simulate blurs caused by slow shutter speed contain more realistic complex dynamic motion. The GoPro dataset contains 3214 blurry/sharp image pairs at 1280×720 resolution, of which 2103 are used for training and the remaining are reserved for evaluation.

HIDE. The HIDE dataset [48] is also a synthetic dataset that is specifically designed for human-aware motion deblurring. The images are collected from a wide range of daily scenes,

covering diverse human motions and complex backgrounds. In this paper, we employ the test dataset containing 2025 pairs of images to evaluate in the motion blur task.

2) *Implementation Details:* Before training the image defocus deblurring, we first preprocess the DPDD dataset as suggested by DPDNet [4]. Specifically, we crop the 1680×1120 image into 512×512 patches by sliding a window striding with 60% overlap. Then, we discard about 30% patches as they are too homogeneous, resulting in adversely affect the training [49]. For the GoPro dataset, we use it as is without extra preprocess.

In training, we empirically use token features of the MAE encoder as transformer features, and set the layer parameter l to 5 by default. For the balance factor λ , we set $\lambda = 1$ in Eq. 5 and $\lambda = 1e-5$ in Eq. 6. In particular, we set the mask ratio of MAE to 50% in the case of the local MAE perceptual loss. For a fair comparison, we train and test the method with the same training dataset under the Pytorch framework. To this end, we reimplement some methods under the Pytorch framework. Since we excel at verifying the proposed perceptual losses on existing learning-based methods, we adopt the same optimizer and train fixed epochs for all comparisons. Considering the RTX 3090 GPU used with 24G memory capacity, we tune down the batch size of some approaches to fit the maximum memory limitation and avoid running out of memory.

3) *Evaluation Metrics:* In order to comprehensively evaluate the effectiveness of our perceptual losses, we calculate both the traditional quantitative quality metrics and the perceptual metrics. For traditional quantitative quality metrics, we calculate PSNR (higher is better), SSIM (higher is better), and MAE (lower is better) metrics between the recovered image and the reference ground truth. For perceptual metrics, we introduce a non-reference metric NIQE (lower is better) [50] and a reference-based metric LPIPS (lower is better) [42]. The NIQE metric is widely used for conditional image generation, indicating the visual realism of generated images. The LPIPS metric is correlated with human perceptual similarity judgments by using deep features in a pretrained VGG.

B. Defocus Deblurring

We select four learning-based methods as our baselines, including DPDNet [4], Uformer-T (abbreviated Uformer in the following sections) [5], Restormer [6], and NAFNet [7], which are the most representative and competitive in the literature. We evaluate different network structures with two different cases: (i) two blurry views of the dual-pixel image pair and (ii) single blurry image. For the dual-pixel defocus deblurring, the quantitative evaluation results and objective comparisons are presented in Fig. 5 and Tab. I. For the single view deblurring, we show visual results in Fig. 6 and objective results in Tab. II.

The results in Tabs. I and II show that training with local MAE perceptual loss provides the most compelling deblurring results in terms of quantitative scores and perceptual metrics. Replacing the feature representation extracted from VGG with those extracted from MAE, the proposed global loss $\mathcal{L}_{percep}^{global}$ produces competitive perceptual and quantitative

results against the classical perceptual loss. Particularly, in term of PSNR, the proposed $\mathcal{L}_{percep}^{local}$ and $\mathcal{L}_{percep}^{global}$ produce significantly better values than the baseline, while showing the superior perceptual performance. On the contrary, model training with classical perceptual loss tends to decrease PSNR scores. Overall, all perceptual losses effectively improve the perceptual quality of deblurred images, where our proposed losses can help the deblurring model recover a more realistic image with better perceptual scores. It demonstrates that in-depth transformer properties are more beneficial for reconstructing high-quality images than the pretrained VGG. In most cases, perceptual losses based on transformer properties lead to performance gains on both quantitation and perception measurement over the baseline.

To further illustrate the advantage of proposed perceptual losses, we show the visual comparison in Figs. 5 and 6. The results recovered by the model trained with $\mathcal{L}_{percep}^{vgg}$ exhibit obvious artifacts as shown in Fig. 5, *e.g.*, the crossed red lines contain obvious noise perturbation. When fed single blurry input, the model guided by $\mathcal{L}_{percep}^{vgg}$ yields over-smooth deblurring results. On the contrary, the models trained with our proposed losses contains more proper structures with fewer artifacts in Fig. 5. When evaluating on the single image deblurring task, the models recover visibly clearer images and much sharper structures under the supervision of our perceptual losses as shown in Fig. 6. As described in Sec. IV-A3 the perceptual metric (LPIPS) appears to suggest a better agreement with humans, where the lower LPIPS score refers to better image quality. Overall, we find that our visual performance is consistent with its objective results, where the model equipped with our perceptual losses yields richer details and achieves better performance in perceptual measurement.

C. Motion Deblurring

To explore the effectiveness of proposed perceptual losses, we evaluate the models on the GoPro and HIDE datasets. In particular, we train the model on the GoPro train dataset and directly test it on HIDE and GoPro test datasets following the experimental settings used in MPRNet [51]. Four representative models are used to evaluate the proposed perceptual losses, including MPRNet [51], Uformer [5], Restormer [6], and NAFNet [7]. In the original four baseline models, they adopt different loss functions: MPRNet is trained with ℓ_1 and an edge regularization term, Uformer is trained with Charbonnier loss [52], Restormer is equipped with ℓ_1 , while NAFNet is equipped with PSNR loss [53]. For fair comparison, we add the proposed perceptual loss as a new regularization term and keep other losses the same as the settings of original papers. In Tab. III and Fig. 7, we present objective comparisons and visual results, respectively.

In objective comparisons, the proposed perceptual losses exhibit advantages over the classical perceptual loss. Specifically, training with the classical perceptual loss $\mathcal{L}_{percep}^{vgg}$, the models (*e.g.*, Uformer, and Restormer) tend to produce the disputing deblurring results where the two perceptual metrics (*i.e.*, LPIPS and NIQE) give inconsistent quality assessment. In addition to perception measurements, the deblurred results generated by the model with classical perceptual loss

TABLE I: Results for the defocus deblurring task on the dual-pixel DPDD dataset [4]. The **bold** numbers indicate the best results and the second bests are marked by underlines.

Method	Loss	Indoor					Outdoor					Combined				
		PSNR	SSIM	MAE	LPIPS	NIQE	PSNR	SSIM	MAE	LPIPS	NIQE	PSNR	SSIM	MAE	LPIPS	NIQE
DPDNet	-	28.05	<u>0.8644</u>	0.0262	0.1341	5.078	22.98	<u>0.7364</u>	<u>0.0514</u>	0.1711	4.370	25.45	<u>0.7987</u>	<u>0.0391</u>	0.1531	4.715
	+ $\mathcal{L}_{percep}^{vgg}$	28.06	0.8615	0.0264	0.0920	4.718	22.85	0.7355	0.0522	0.1376	4.046	25.39	0.7969	0.0396	0.1154	4.373
	+ $\mathcal{L}_{percep}^{local}$	28.57	0.8652	0.0258	0.0766	4.990	23.35	0.7375	0.0501	0.1114	4.338	25.88	0.7997	0.0382	0.0945	4.656
	+ $\mathcal{L}_{percep}^{global}$	<u>28.11</u>	0.8593	<u>0.0261</u>	<u>0.0902</u>	4.751	<u>23.02</u>	0.7343	<u>0.0514</u>	<u>0.1358</u>	<u>4.129</u>	<u>25.50</u>	0.7952	<u>0.0391</u>	<u>0.1049</u>	<u>4.432</u>
Uformer	-	28.59	0.8733	0.0251	0.1279	5.123	23.48	0.7524	0.0493	0.1672	4.306	25.97	0.8111	0.0375	0.1480	4.704
	+ $\mathcal{L}_{percep}^{vgg}$	28.61	0.8760	0.0253	0.1085	5.042	23.56	0.7544	0.0490	0.1519	4.190	26.02	0.8135	0.0375	0.1308	4.605
	+ $\mathcal{L}_{percep}^{local}$	28.84	0.8788	0.0246	0.0771	<u>4.865</u>	23.68	0.7611	0.0482	0.1187	<u>4.083</u>	26.20	0.8184	0.0367	0.0985	<u>4.464</u>
	+ $\mathcal{L}_{percep}^{global}$	<u>28.73</u>	<u>0.8763</u>	<u>0.0248</u>	<u>0.0820</u>	4.685	<u>23.56</u>	<u>0.7551</u>	<u>0.0489</u>	<u>0.1265</u>	3.950	<u>26.08</u>	<u>0.8141</u>	<u>0.0371</u>	<u>0.1048</u>	4.307
Restormer	-	29.06	<u>0.8850</u>	0.0233	0.1318	5.451	23.67	0.7647	0.0481	0.1506	4.668	26.29	<u>0.8232</u>	0.0360	0.1414	5.049
	+ $\mathcal{L}_{percep}^{vgg}$	29.17	0.8858	0.0231	0.1042	5.203	23.66	0.7628	0.0482	0.1323	4.410	26.34	0.8227	<u>0.0359</u>	0.1186	4.796
	+ $\mathcal{L}_{percep}^{local}$	29.17	0.8839	0.0235	0.0689	4.929	23.84	0.7660	0.0473	0.0999	<u>4.248</u>	26.43	0.8234	0.0357	0.0848	<u>4.579</u>
	+ $\mathcal{L}_{percep}^{global}$	<u>29.11</u>	0.8829	<u>0.0232</u>	<u>0.0775</u>	<u>4.934</u>	<u>23.72</u>	<u>0.7651</u>	<u>0.0480</u>	<u>0.1113</u>	4.231	<u>26.35</u>	0.8224	<u>0.0359</u>	<u>0.0949</u>	4.573
NAFNet	-	<u>29.21</u>	0.8875	0.0234	0.1230	5.295	23.81	0.7665	0.0480	0.1558	4.491	26.44	<u>0.8254</u>	0.0360	0.1399	4.883
	+ $\mathcal{L}_{percep}^{vgg}$	29.09	<u>0.8857</u>	0.0238	0.1122	5.239	23.81	<u>0.7678</u>	0.0480	0.1453	4.371	26.38	0.8251	0.0362	0.1292	4.793
	+ $\mathcal{L}_{percep}^{local}$	29.24	0.8848	<u>0.0235</u>	0.0672	4.832	23.95	0.7701	0.0468	0.1024	4.091	26.53	0.8259	0.0355	0.0852	4.451
	+ $\mathcal{L}_{percep}^{global}$	29.17	0.8850	<u>0.0235</u>	<u>0.0764</u>	<u>4.910</u>	<u>23.86</u>	0.7671	<u>0.0477</u>	<u>0.1168</u>	<u>4.253</u>	<u>26.45</u>	0.8245	<u>0.0359</u>	<u>0.0971</u>	<u>4.572</u>

show worse quantitative scores compared to baseline models w.r.t. MPRNet, Uformer, and Restormer. In contrast, models equipped with our proposed perceptual losses consistently perform better perceptual quality scores than baselines. Furthermore, in term of PSNR, our perceptual losses show competitive performance against the baseline on the MPRNet and go beyond other counterparts on Uformer, Restormer, and NAFNet. Overall, our proposed losses are effective on the motion deblurring task, which is thoroughly demonstrated on the HIDE and GoPro datasets.

For visual comparisons, we present an example from GoPro test dataset as shown in Fig. 7. The models regularized with $\mathcal{L}_{percep}^{vgg}$ recover low-contrast images, showing a color shift to some extent. To better highlight the missing details, we also provide the visualization of residual maps between deblurring results and ground truth. It can be seen that our perceptual losses, especially for $\mathcal{L}_{percep}^{local}$, have a tendency to yield a perceptually pleasing and sharp images with fewer artifacts. Since both objective and visual comparisons reveal that the proposed perceptual losses are effective for the motion deblurring task, it demonstrates that our losses are robust to various and complex blurred scenes.

D. Ablation Study

In this section, we first study which type of pretrained ViT is more effective in guiding the image deblurring tasks (Sec. IV-D1). Then, we analyze the effects of different feature representations in ViT in Sec. IV-D2. Finally, we discuss the setting of key hyperparameters (*i.e.*, layer number of feature extraction and mask ratio) in Sec. IV-D3. For convenience, all ablation studies are carried out with the DPDNet and regularized with local MAE perceptual loss $\mathcal{L}_{percep}^{local}$ on the dual-pixel defocus deblurring task.

1) *MAE, DINO, and ViT*: In this section, we compare three representative ViT architectures on the DPDD dataset. The three pretrained ViTs contain almost the same architecture but quite different parameters. The first type is the vanilla vision transformer obtained from supervised learning, which is marked as ViT [17]. The second and third types, called DINO [43] and MAE [44], respectively, are based on self-supervised learning frameworks. The comparison results are summarized in Tab. IV.

The results in Tab. IV show that the MAE outperforms other types of ViTs on all metrics. Specifically, compared to the baseline in term of PSNR, the MAE achieves a marginal improvement of 0.43 dB in term of PSNR, while DINO and vanilla ViT demonstrate similar slight performance gains (approximately 0.12 dB \sim 0.16 dB). In addition to PSNR, the LPIPS score of MAE also outperforms the counterparts by a large margin, indicating that the feature representations of MAE facilitate the deblurring model to produce images of high perceptual quality. Another intriguing observation is that ViTs trained in self-supervised learning way perform consistently improvements under both quantitative and perception measurement. In the following ablation studies, we set the MAE to the default setting due to its impressive performance.

2) *Feature Representation*: In the previous ablation study, we have analyzed the benefits of pretrained parameters among different types of ViT. Here, we further study which types of feature representations (*i.e.*, key, query, value, and token) are more efficient in Sec. III-B. As present in Tab. V, it is obvious that no one type of feature representation has absolute advantages over their counterparts in all metrics. When the query/value features are used for the guidance, the obtained PSNR and MAE scores significantly go beyond those of the baseline. However, the NIQE scores suggest that using

TABLE II: Results for defocus deblurring task on the DPDD dataset [4]. The **bold** numbers indicate the best results and the second bests are marked by underlines.

Method	Loss	Indoor					Outdoor					Combined				
		PSNR	SSIM	MAE	LPIPS	NIQE	PSNR	SSIM	MAE	LPIPS	NIQE	PSNR	SSIM	MAE	LPIPS	NIQE
DPDNet	-	27.46	<u>0.8420</u>	0.0280	0.1675	5.3151	22.26	0.6920	0.0553	0.2167	4.6339	24.79	0.7650	0.0420	0.1928	4.9655
	$+\mathcal{L}_{percep}^{vgg}$	27.39	0.8426	0.0283	0.1138	<u>4.8428</u>	22.21	0.6920	0.0555	0.1801	<u>4.1922</u>	24.73	0.7653	0.0423	0.1478	<u>4.5089</u>
	$+\mathcal{L}_{percep}^{local}$	<u>27.53</u>	0.8418	0.0277	<u>0.1071</u>	4.8961	22.39	0.6954	0.0544	<u>0.1716</u>	4.2747	24.89	0.7667	0.0414	<u>0.1402</u>	4.5772
	$+\mathcal{L}_{percep}^{global}$	27.55	0.8398	<u>0.0278</u>	0.1070	4.6802	<u>22.29</u>	<u>0.6949</u>	<u>0.0551</u>	0.1708	4.0564	<u>24.85</u>	<u>0.7654</u>	<u>0.0418</u>	0.1398	4.3601
Uformer	-	27.90	0.8573	0.0265	0.1427	5.1928	22.56	0.7187	0.0538	0.1873	4.3566	25.16	0.7862	0.0405	0.1656	4.7637
	$+\mathcal{L}_{percep}^{vgg}$	27.86	<u>0.8604</u>	0.0265	0.1298	5.1113	22.68	<u>0.7213</u>	<u>0.0530</u>	0.1787	4.2743	25.20	<u>0.7890</u>	0.0401	0.1549	4.6818
	$+\mathcal{L}_{percep}^{local}$	28.17	0.8634	0.0259	0.0797	<u>4.8137</u>	22.85	0.7257	0.0519	0.1297	4.0440	25.44	0.7928	0.0392	0.1054	4.4187
	$+\mathcal{L}_{percep}^{global}$	27.94	0.8568	<u>0.0264</u>	<u>0.0944</u>	4.8131	22.67	0.7184	<u>0.0530</u>	<u>0.1526</u>	4.1799	25.24	0.7857	<u>0.0400</u>	<u>0.1243</u>	<u>4.4882</u>
Restormer	-	28.27	0.8631	<u>0.0254</u>	0.1435	5.4370	22.91	0.7143	<u>0.0511</u>	0.2032	4.9121	25.52	0.7868	0.0386	0.1741	5.1676
	$+\mathcal{L}_{percep}^{vgg}$	<u>28.32</u>	0.8626	0.0256	0.1411	5.3994	22.89	0.7143	0.0510	0.1908	4.8744	25.54	0.7865	0.0386	0.1666	5.1300
	$+\mathcal{L}_{percep}^{local}$	28.56	0.8688	0.0253	0.0854	4.9113	<u>22.94</u>	<u>0.7220</u>	0.0514	0.1307	4.4031	25.68	0.7935	<u>0.0387</u>	0.1086	4.6505
	$+\mathcal{L}_{percep}^{global}$	<u>28.32</u>	<u>0.8645</u>	0.0256	<u>0.1102</u>	5.1762	23.00	0.7233	<u>0.0511</u>	<u>0.1646</u>	4.6384	<u>25.59</u>	<u>0.7920</u>	<u>0.0387</u>	<u>0.1381</u>	<u>4.9002</u>
NAFNet	-	28.16	0.8651	0.0257	0.1365	5.3256	22.75	<u>0.7231</u>	0.0526	0.1861	4.5713	25.38	0.7922	0.0395	0.1619	4.9385
	$+\mathcal{L}_{percep}^{vgg}$	<u>28.20</u>	0.8671	<u>0.0257</u>	0.1250	5.2839	22.73	0.7230	0.0528	0.1751	4.3924	25.39	0.7932	0.0396	0.1507	4.8265
	$+\mathcal{L}_{percep}^{local}$	28.42	<u>0.8664</u>	0.0249	0.0781	4.9439	22.88	0.7237	0.0517	0.1299	4.0781	25.58	<u>0.7931</u>	0.0387	0.1047	4.4996
	$+\mathcal{L}_{percep}^{global}$	28.18	0.8612	<u>0.0257</u>	<u>0.0890</u>	<u>4.9993</u>	<u>22.80</u>	0.7198	<u>0.0525</u>	<u>0.1468</u>	<u>4.3917</u>	<u>25.42</u>	0.7887	<u>0.0395</u>	<u>0.1187</u>	<u>4.6875</u>

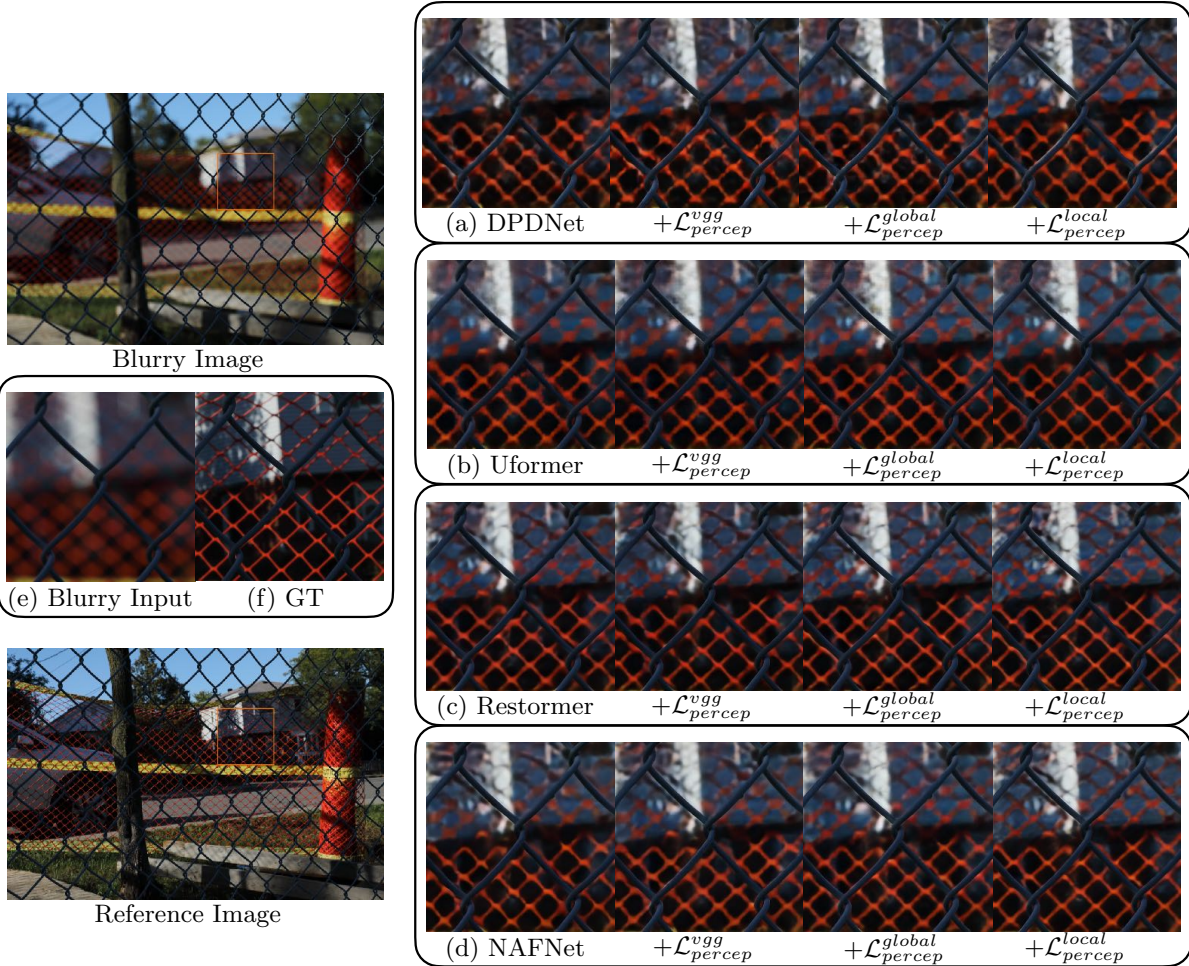


Fig. 5: A visual example on the dual-pixel DPDD dataset. For convenience, we show only the left view as the blurry image. From (a) to (d), we present cropped highlighted deblurring results to validate the effectiveness of proposed perceptual losses on DPDNet, Uformer, Restormer, and NAFNet, respectively.

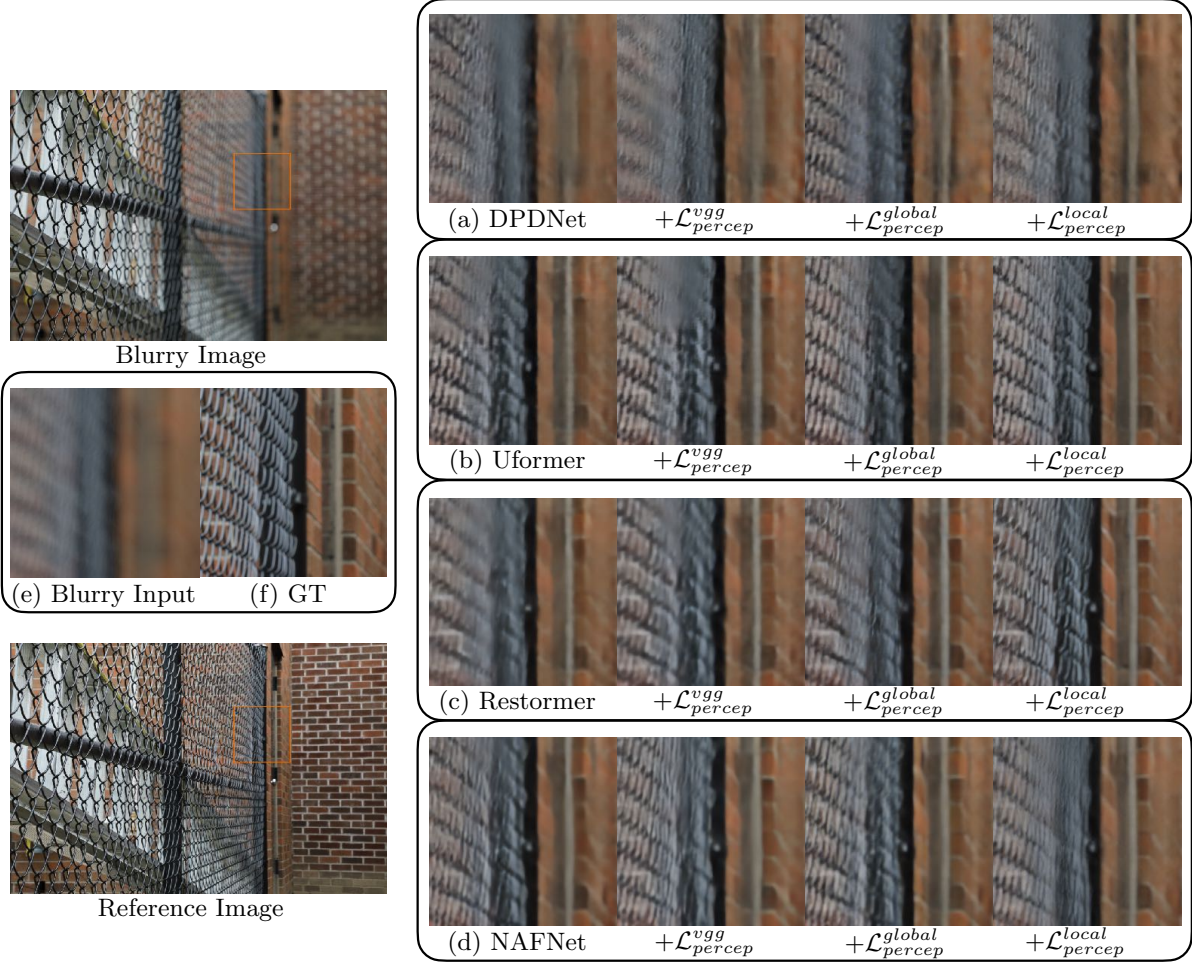


Fig. 6: Visual comparison of a single blurry image on the DPDD test dataset. From (a) to (d), we present cropped highlighted deblurring results to validate the effectiveness of proposed perceptual losses on DPDNet, Uformer, Restormer, and NAFNet, respectively.

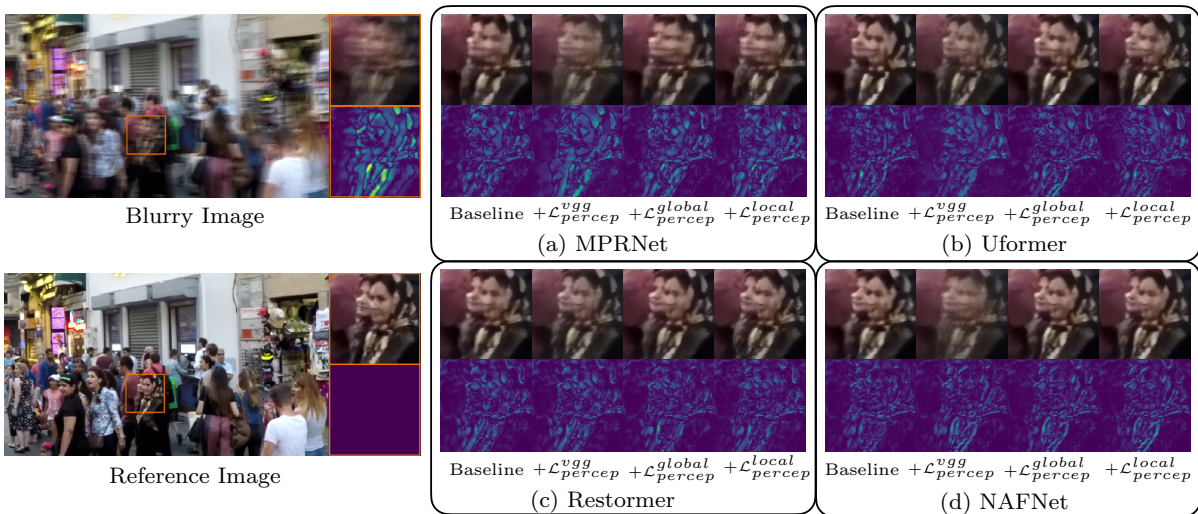


Fig. 7: Visual comparisons of the motion deblurring task on the GoPro test dataset [28]. To better highlight the differences, we visualize the residual maps between recovered patches and reference in (a)-(d).

TABLE III: Results on the GoPro dataset [28] and the HIDE [48] for motion deblurring task. The **bold** numbers indicate the best results and the second bests are marked by underscores.

Method	Loss	GoPro				HIDE			
		PSNR	SSIM	LPIPS	NIQE	PSNR	SSIM	LPIPS	NIQE
MPRNet	-	28.55	0.9111	0.1343	5.4627	27.25	0.8847	0.1425	4.9244
	$+\mathcal{L}_{percep}^{vgg}$	28.15	0.9040	0.0876	4.7615	27.09	0.8792	0.1073	4.1345
	$+\mathcal{L}_{percep}^{local}$	28.47	<u>0.9093</u>	<u>0.1102</u>	<u>4.9845</u>	27.12	0.8818	<u>0.1250</u>	<u>4.3741</u>
	$+\mathcal{L}_{percep}^{global}$	<u>28.48</u>	<u>0.9093</u>	0.1145	5.1228	<u>27.18</u>	<u>0.8824</u>	0.1282	4.6510
Uformer	-	30.21	<u>0.9343</u>	0.1135	5.5583	28.48	<u>0.9079</u>	0.1296	4.9227
	$+\mathcal{L}_{percep}^{vgg}$	29.72	0.9197	<u>0.0694</u>	5.9382	28.09	0.8820	<u>0.0920</u>	5.7450
	$+\mathcal{L}_{percep}^{local}$	<u>30.21</u>	0.9311	0.0652	4.3113	<u>28.54</u>	0.9009	0.0865	3.8116
	$+\mathcal{L}_{percep}^{global}$	30.24	0.9346	0.0787	<u>4.8536</u>	28.55	0.9080	0.0979	<u>4.3274</u>
Restormer	-	29.61	0.9277	0.1154	5.4515	28.62	<u>0.9109</u>	0.1225	4.9703
	$+\mathcal{L}_{percep}^{vgg}$	29.59	0.9193	<u>0.0639</u>	5.5767	28.18	0.8848	<u>0.0848</u>	5.4517
	$+\mathcal{L}_{percep}^{local}$	30.00	0.9315	0.0620	4.5327	<u>28.70</u>	0.9099	0.0791	3.8731
	$+\mathcal{L}_{percep}^{global}$	30.00	0.9332	0.0718	<u>4.7452</u>	28.71	0.9116	0.0887	<u>4.1751</u>
NAFNet	-	32.40	0.9565	0.0847	5.2740	30.18	0.9304	0.0954	4.6582
	$+\mathcal{L}_{percep}^{vgg}$	<u>32.60</u>	<u>0.9580</u>	<u>0.0590</u>	4.9712	30.37	0.9328	0.0761	4.2791
	$+\mathcal{L}_{percep}^{local}$	32.64	0.9582	0.0557	<u>4.9093</u>	30.37	<u>0.9322</u>	0.0722	<u>4.1120</u>
	$+\mathcal{L}_{percep}^{global}$	32.48	0.9568	0.0557	4.7807	<u>30.19</u>	0.9279	<u>0.0738</u>	4.0281

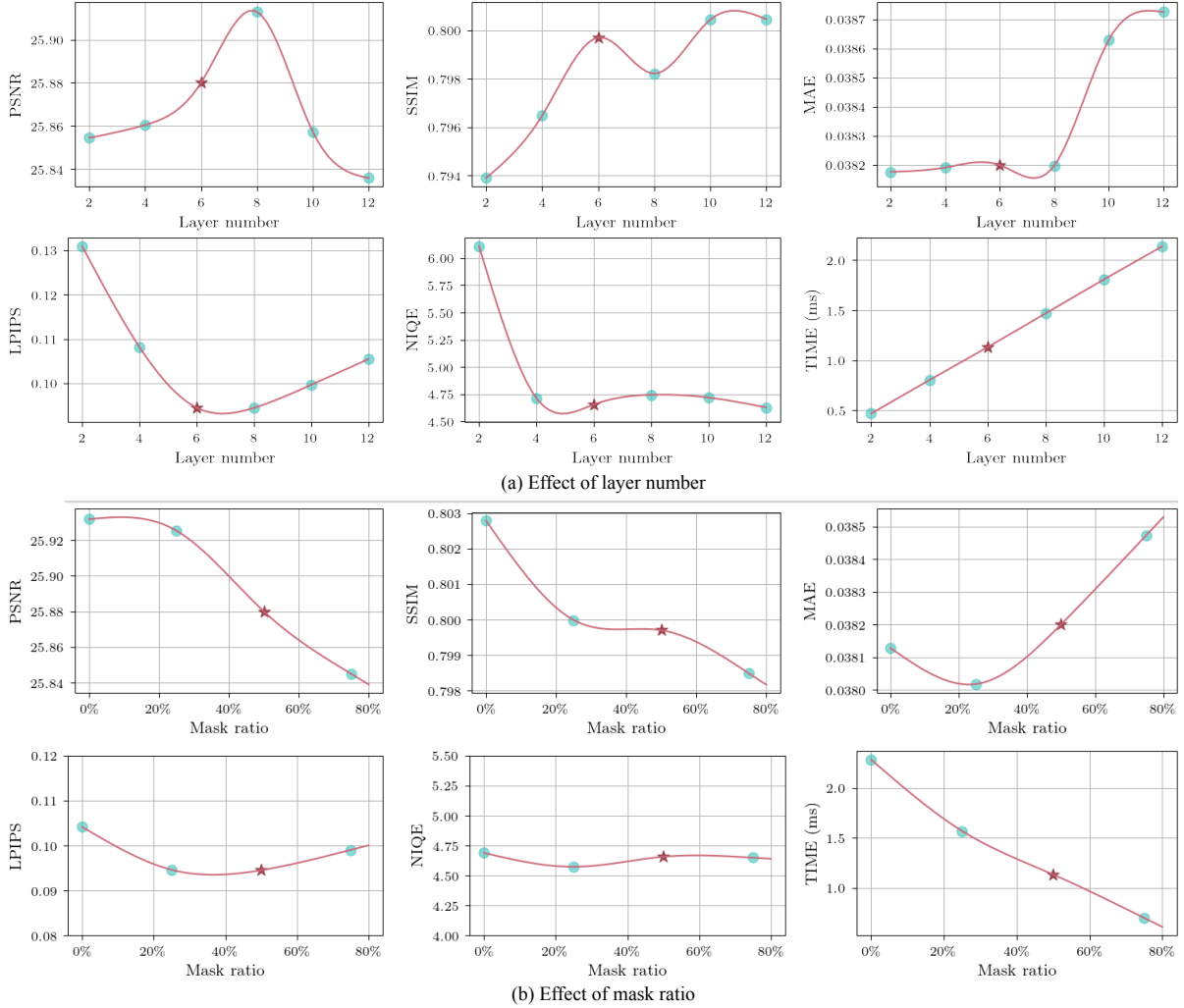


Fig. 8: Effect of the hyperparameter setting of the MAE encoder. In the first two rows, we report the quantitative comparisons and time-consuming result when features are extracted from different layer numbers. In the last two rows, we depict the quantitative comparisons and time-consuming results in different mask ratio cases. Default setting is marked as \star in the subplots.

TABLE IV: Evaluation of the impact of the types of pretrained ViTs. We notate the pretrained vanilla vision transformer based on supervised learning as ViT, and simplify the DINO-ViT as DINO. The reported baseline originates from the DPDNet trained on the dual-pixel DPDD dataset. The default settings are marked in gray .

Type	PSNR	SSIM	MAE	LPIPS	NIQE
Baseline	25.45	<u>0.7987</u>	0.0391	0.1531	4.715
ViT	<u>25.61</u>	0.7967	<u>0.0389</u>	<u>0.1237</u>	4.675
DINO	25.57	<u>0.7987</u>	0.0390	0.1241	<u>4.667</u>
MAE	25.88	0.7997	0.0382	0.0945	4.656

TABLE V: Evaluation of the impact of the types of feature representations. The reported baseline originates from the DPDNet trained on the dual-pixel DPDD dataset. The default settings are marked in gray .

Type	PSNR	SSIM	MAE	LPIPS	NIQE
Baseline	25.45	<u>0.7987</u>	0.0391	0.1531	4.715
Key	25.84	0.7956	<u>0.0381</u>	0.0955	4.626
Query	<u>25.90</u>	0.7966	0.0379	0.0942	4.756
Value	25.96	0.7986	0.0379	0.0983	4.731
Token	25.88	0.7997	0.0382	<u>0.0945</u>	<u>4.656</u>

the query/value features performs worse than the baseline. Therefore, it is hard to determine which type of feature is beneficial or useless. The key features suffer from the similar problem that the model taking key features as regularization term shows a significant improvement of perceptual quality while performing poorly measured by quantitative metrics (e.g., SSIM). Considering the balance between perceptual quality and quantitative scores, we employ token features as the default feature representations for our perceptual losses. It is worth noting that the model trained with token features demonstrates comprehensive performance gains compared to the baseline.

3) *MAE Encoder*: The ablation studies conducted in this section excel in investigating the impact of key hyperparameter choices in MAE. Here, we analyze two key factors: 1) layer number; 2) mask ratio. For the layer number, we have discussed in Sec. III-B, which refers to the l -th transformer layer used to extract features. The mask ratio indicates that a portion of tokens is randomly masking in the input. Visual comparison results are shown in Fig. 8.

Layer number. To intuitively illustrate the impact of layer number of the pretrained features, we present a smooth curve to fit the discrete measurement scores of different layers, as shown in Fig. 8. We observe that the image quality scores do not vary monotonically as the layer number increases. The optimal results always appear in the middle layer instead of in the beginning or end layer. Another intriguing observation is that the middle layers, e.g., 6th and 8th, tend to produce

results with both a better quantitative and perceptual quality. Therefore, it can be concluded that the features extracted from the middle layers of the MAE play a more important role in guiding the deblurring task. Furthermore, for the running time, it is clear that the time cost is linear with the layer depth, that is, the deeper the layer, the more time is consumed.

Mask ratio. Mask ratio is a vital parameter for MAE, and the model with proper mask ratio will obtain robust and powerful features. Here, we analyze the mask ratio to explore its impact on deblurring performance. Fig. 8 shows the comparison results in the cases where we set the mask ratio to 0%, 25%, 50%, 75%, respectively. As can be seen, the varying of mask ratio has not obvious impact on the perceptual quality compared to the cases of layer number. This demonstrates that the information of extracted features is redundant for image deblurring to some extent. In addition, for the running time, we observe that time-consuming does not linearly increase as the mask ratio decreases. We set the mask ratio to 50% as a default setting considering running efficiency and performance improvement.

V. CONCLUSION

In this paper, we explore harnessing the in-depth transformer properties into image deblurring tasks. To accomplish this, we propose two types of perceptual losses: the local MAE perceptual loss and the global distribution perceptual loss. The former is to directly measure the feature distance in Euclidean space, whereas the latter is defined by comparing the feature distributions. We analyze the effectiveness of proposed perceptual losses on multiple mainstream image deblurring tasks, including dual-pixel defocus deblurring and motion deblurring. Experiments show that the perceptual losses using transformer properties achieve noticeable performance improvement over various baselines and classical perceptual loss based on VGG.

REFERENCES

- [1] K. Zhang, W. Ren, W. Luo, W.-S. Lai, B. Stenger, M.-H. Yang, and H. Li, "Deep image deblurring: A survey," *International Journal of Computer Vision*, pp. 2103–2130, 2022.
- [2] J. Shi, L. Xu, and J. Jia, "Discriminative blur detection features," in *Proceedings of the IEEE Conference on Computer Vision and Pattern Recognition*, 2014, pp. 2965–2972.
- [3] T. Hyun Kim and K. Mu Lee, "Generalized video deblurring for dynamic scenes," in *Proceedings of the IEEE Conference on Computer Vision and Pattern Recognition*, 2015, pp. 5426–5434.
- [4] A. Abuolaim and M. S. Brown, "Defocus deblurring using dual-pixel data," in *Proceedings of the European Conference on Computer Vision*. Springer, 2020, pp. 111–126.
- [5] Z. Wang, X. Cun, J. Bao, W. Zhou, J. Liu, and H. Li, "Uformer: A general u-shaped transformer for image restoration," in *Proceedings of the IEEE Conference on Computer Vision and Pattern Recognition*, 2022, pp. 17 683–17 693.
- [6] S. W. Zamir, A. Arora, S. Khan, M. Hayat, F. S. Khan, and M.-H. Yang, "Restormer: Efficient transformer for high-resolution image restoration," in *Proceedings of the IEEE/CVF Conference on Computer Vision and Pattern Recognition*, 2022, pp. 5728–5739.
- [7] L. Chen, X. Chu, X. Zhang, and J. Sun, "Simple baselines for image restoration," in *Proceedings of the European Conference on Computer Vision*, 2022.
- [8] P. Liang, J. Jiang, X. Liu, and J. Ma, "Bambnet: A blur-aware multi-branch network for dual-pixel defocus deblurring," *IEEE/CAA Journal of Automatica Sinica*, vol. 9, no. 5, pp. 878–892, 2022.
- [9] J. Johnson, A. Alahi, and L. Fei-Fei, "Perceptual losses for real-time style transfer and super-resolution," in *Proceedings of the European Conference on Computer Vision*. Springer, 2016, pp. 694–711.

- [10] S. Nah, S. Son, J. Lee, and K. M. Lee, "Clean images are hard to reblur: Exploiting the ill-posed inverse task for dynamic scene deblurring," in *International Conference on Learning Representations*, 2021.
- [11] M. Delbracio, H. Talebei, and P. Milanfar, "Projected distribution loss for image enhancement," in *Proceedings of the IEEE International Conference on Computational Photography*. IEEE Computer Society, may 2021, pp. 1–12.
- [12] C. Ledig, L. Theis, F. Huszár, J. Caballero, A. Cunningham, A. Acosta, A. Aitken, A. Tejani, J. Totz, Z. Wang *et al.*, "Photo-realistic single image super-resolution using a generative adversarial network," in *Proceedings of the IEEE Conference on Computer Vision and Pattern Recognition*, 2017, pp. 4681–4690.
- [13] O. Kupyn, T. Martyniuk, J. Wu, and Z. Wang, "Deblurgan-v2: Deblurring (orders-of-magnitude) faster and better," in *Proceedings of the IEEE International Conference on Computer Vision*, 2019, pp. 8878–8887.
- [14] K. Zhang, W. Luo, Y. Zhong, L. Ma, B. Stenger, W. Liu, and H. Li, "Deblurring by realistic blurring," in *Proceedings of the IEEE Conference on Computer Vision and Pattern Recognition*, 2020, pp. 2737–2746.
- [15] S. Amir, Y. Gandelsman, S. Bagon, and T. Dekel, "Deep vit features as dense visual descriptors," *arXiv preprint arXiv:2112.05814*, 2021.
- [16] H. Chen, Y. Wang, T. Guo, C. Xu, Y. Deng, Z. Liu, S. Ma, C. Xu, C. Xu, and W. Gao, "Pre-trained image processing transformer," in *Proceedings of the IEEE Conference on Computer Vision and Pattern Recognition*, 2021, pp. 12299–12310.
- [17] A. Dosovitskiy, L. Beyer, A. Kolesnikov, D. Weissenborn, X. Zhai, T. Unterthiner, M. Dehghani, M. Minderer, G. Heigold, S. Gelly, J. Uszkoreit, and N. Houlsby, "An image is worth 16x16 words: Transformers for image recognition at scale," *Proceedings of the International Conference on Learning Representations*, 2021.
- [18] N. Tumanyan, O. Bar-Tal, S. Bagon, and T. Dekel, "Splicing vit features for semantic appearance transfer," in *Proceedings of the IEEE Conference on Computer Vision and Pattern Recognition*, 2022, pp. 2737–2746.
- [19] C. Villani, *Optimal transport: old and new*. Springer, 2009, vol. 338.
- [20] A. Abuolaim, M. Delbracio, D. Kelly, M. S. Brown, and P. Milanfar, "Learning to reduce defocus blur by realistically modeling dual-pixel data," in *Proceedings of the IEEE Conference on Computer Vision and Pattern Recognition*, 2021.
- [21] S. Xin, N. Wadhwa, T. Xue, J. T. Barron, P. P. Srinivasan, J. Chen, I. Gkioulekas, and R. Garg, "Defocus map estimation and deblurring from a single dual-pixel image," in *Proceedings of the IEEE International Conference on Computer Vision*, 2021, pp. 2228–2238.
- [22] J. Lee, H. Son, J. Rim, S. Cho, and S. Lee, "Iterative filter adaptive network for single image defocus deblurring," in *Proceedings of the IEEE Conference on Computer Vision and Pattern Recognition*, 2021.
- [23] H. Son, J. Lee, S. Cho, and S. Lee, "Single image defocus deblurring using kernel-sharing parallel atrous convolutions," in *Proceedings of the IEEE International Conference on Computer Vision*, 2021, pp. 2642–2650.
- [24] L. Ruan, B. Chen, J. Li, and M. Lam, "Learning to deblur using light field generated and real defocus images," in *Proceedings of the IEEE/CVF Conference on Computer Vision and Pattern Recognition*, 2022, pp. 16304–16313.
- [25] D. Gong, Z. Zhang, Q. Shi, A. van den Hengel, C. Shen, and Y. Zhang, "Learning deep gradient descent optimization for image deconvolution," *IEEE Transactions on Neural Networks and Learning Systems*, vol. 31, no. 12, pp. 5468–5482, 2020.
- [26] L. Pan, S. Chowdhury, R. Hartley, M. Liu, H. Zhang, and H. Li, "Dual pixel exploration: Simultaneous depth estimation and image restoration," in *Proceedings of the IEEE Conference on Computer Vision and Pattern Recognition*, 2021, pp. 4340–4349.
- [27] H. Ma, S. Liu, Q. Liao, J. Zhang, and J.-H. Xue, "Defocus image deblurring network with defocus map estimation as auxiliary task," *IEEE Transactions on Image Processing*, vol. 31, pp. 216–226, 2021.
- [28] S. Nah, T. Hyun Kim, and K. Mu Lee, "Deep multi-scale convolutional neural network for dynamic scene deblurring," in *Proceedings of the IEEE Conference on Computer Vision and Pattern Recognition*, 2017, pp. 3883–3891.
- [29] Y. Liu, F. Fang, T. Wang, J. Li, Y. Sheng, and G. Zhang, "Multi-scale grid network for image deblurring with high-frequency guidance," *IEEE Transactions on Multimedia*, 2021.
- [30] X. Tao, H. Gao, X. Shen, J. Wang, and J. Jia, "Scale-recurrent network for deep image deblurring," in *Proceedings of the IEEE Conference on Computer Vision and Pattern Recognition*, 2018.
- [31] H. Gao, X. Tao, X. Shen, and J. Jia, "Dynamic scene deblurring with parameter selective sharing and nested skip connections," in *Proceedings of the IEEE/CVF conference on computer vision and pattern recognition*, 2019, pp. 3848–3856.
- [32] O. Kupyn, V. Budzan, M. Mykhailych, D. Mishkin, and J. Matas, "Deblurgan: Blind motion deblurring using conditional adversarial networks," in *Proceedings of the IEEE Conference on Computer Vision and Pattern Recognition*, 2018, pp. 8183–8192.
- [33] O. Kupyn, T. Martyniuk, J. Wu, and Z. Wang, "Deblurgan-v2: Deblurring (orders-of-magnitude) faster and better," in *Proceedings of the IEEE International Conference on Computer Vision*, 2019, pp. 8878–8887.
- [34] Y. Wen, J. Chen, B. Sheng, Z. Chen, P. Li, P. Tan, and T.-Y. Lee, "Structure-aware motion deblurring using multi-adversarial optimized cyclegan," *IEEE Transactions on Image Processing*, vol. 30, pp. 6142–6155, 2021.
- [35] J. Zhang and W. Zhai, "Blind attention geometric restraint neural network for single image dynamic/defocus deblurring," *IEEE Transactions on Neural Networks and Learning Systems*, 2022.
- [36] X. Mao, Y. Liu, W. Shen, Q. Li, and Y. Wang, "Deep residual fourier transformation for single image deblurring," *arXiv*, 2021.
- [37] Y. Bahat, N. Efrat, and M. Irani, "Non-uniform blind deblurring by reblurring," in *Proceedings of the IEEE International Conference on Computer Vision*, 2017, pp. 3286–3294.
- [38] H. Chen, M. Teng, B. Shi, Y. Wang, and T. Huang, "A residual learning approach to deblur and generate high frame rate video with an event camera," *IEEE Transactions on Multimedia*, 2022.
- [39] S.-J. Cho, S.-W. Ji, J.-P. Hong, S.-W. Jung, and S.-J. Ko, "Rethinking coarse-to-fine approach in single image deblurring," in *Proceedings of the IEEE International Conference on Computer Vision*, 2021.
- [40] X. Zhang, R. Ng, and Q. Chen, "Single image reflection separation with perceptual losses," in *Proceedings of the IEEE Conference on Computer Vision and Pattern Recognition*, 2018, pp. 4786–4794.
- [41] H. Zhang, V. Sindagi, and V. M. Patel, "Multi-scale single image dehazing using perceptual pyramid deep network," in *Proceedings of the IEEE Conference on Computer Vision and Pattern Recognition Workshops*, 2018, pp. 902–911.
- [42] R. Zhang, P. Isola, A. A. Efros, E. Shechtman, and O. Wang, "The unreasonable effectiveness of deep features as a perceptual metric," in *Proceedings of the IEEE Conference on Computer Vision and Pattern Recognition*, 2018, pp. 586–595.
- [43] M. Caron, H. Touvron, I. Misra, H. Jégou, J. Mairal, P. Bojanowski, and A. Joulin, "Emerging properties in self-supervised vision transformers," in *Proceedings of the IEEE International Conference on Computer Vision*, 2021, pp. 9650–9660.
- [44] K. He, X. Chen, S. Xie, Y. Li, P. Dollár, and R. Girshick, "Masked autoencoders are scalable vision learners," in *Proceedings of the IEEE Conference on Computer Vision and Pattern Recognition*, 2022, pp. 16000–16009.
- [45] M. M. Naseer, K. Ranasinghe, S. H. Khan, M. Hayat, F. Shahbaz Khan, and M.-H. Yang, "Intriguing properties of vision transformers," *Advances in Neural Information Processing Systems*, vol. 34, pp. 23 296–23 308, 2021.
- [46] S. Cao, P. Xu, and D. A. Clifton, "How to understand masked autoencoders," *arXiv preprint arXiv:2202.03670*, 2022.
- [47] V. M. Panaretos and Y. Zemel, "Statistical aspects of wasserstein distances," *Annual Review of Statistics and Its Application*, vol. 6, no. 1, pp. 405–431, 2019.
- [48] Z. Shen, W. Wang, X. Lu, J. Shen, H. Ling, T. Xu, and L. Shao, "Human-aware motion deblurring," in *Proceedings of the IEEE/CVF International Conference on Computer Vision*, 2019, pp. 5572–5581.
- [49] J. Park, Y.-W. Tai, D. Cho, and I. So Kweon, "A unified approach of multi-scale deep and hand-crafted features for defocus estimation," in *Proceedings of the IEEE Conference on Computer Vision and Pattern Recognition*, 2017, pp. 1736–1745.
- [50] A. Mittal, R. Soundararajan, and A. C. Bovik, "Making a "completely blind" image quality analyzer," *IEEE Signal processing letters*, vol. 20, no. 3, pp. 209–212, 2012.
- [51] S. W. Zamir, A. Arora, S. Khan, M. Hayat, F. S. Khan, M.-H. Yang, and L. Shao, "Multi-stage progressive image restoration," in *Proceedings of the IEEE Conference on Computer Vision and Pattern Recognition*, 2021, pp. 14 821–14 831.
- [52] —, "Learning enriched features for real image restoration and enhancement," in *European Conference on Computer Vision*. Springer, 2020, pp. 492–511.
- [53] L. Chen, X. Lu, J. Zhang, X. Chu, and C. Chen, "Hinet: Half instance normalization network for image restoration," in *Proceedings of the IEEE Conference on Computer Vision and Pattern Recognition*, 2021, pp. 182–192.